Impinging laminar jets at moderate Reynolds numbers and separation distances

Jeffrey M. Bergthorson,* Kazuo Sone, Trent W. Mattner, Paul E. Dimotakis, David G. Goodwin, and Dan I. Meiron
California Institute of Technology, Pasadena, California 91125, USA
(Received 7 June 2005; published 14 December 2005)

An experimental and numerical study of impinging, incompressible, axisymmetric, laminar jets is described, where the jet axis of symmetry is aligned normal to the wall. Particle streak velocimetry (PSV) is used to measure axial velocities along the centerline of the flow field. The jet-nozzle pressure drop is measured simultaneously and determines the Bernoulli velocity. The flow field is simulated numerically by an axisymmetric Navier-Stokes spectral-element code, an axisymmetric potential-flow model, and an axisymmetric one-dimensional stream-function approximation. The axisymmetric viscous and potential-flow simulations include the nozzle in the solution domain, allowing nozzle-wall proximity effects to be investigated. Scaling the centerline axial velocity by the Bernoulli velocity collapses the experimental velocity profiles onto a single curve that is independent of the nozzle-to-plate separation distance. Axisymmetric direct numerical simulations yield good agreement with experiment and confirm the velocity profile scaling. Potential-flow simulations reproduce the collapse of the data; however, viscous effects result in disagreement with experiment. Axisymmetric one-dimensional stream-function simulations can predict the flow in the stagnation region if the boundary conditions are correctly specified. The scaled axial velocity profiles are well characterized by an error function with one Reynolds-number-dependent parameter. Rescaling the wall-normal distance by the boundary-layer displacement-thickness-corrected diameter yields a collapse of the data onto a single curve that is independent of the Reynolds number. These scalings allow the specification of an analytical expression for the velocity profile of an impinging laminar jet over the Reynolds number range investigated of $200 \leqslant \mathrm{Re} \leqslant 1400$.

DOI: 10.1103/PhysRevE.72.066307 PACS number(s): 47.15.−x

I. INTRODUCTION

Axisymmetric jets impinging perpendicularly on a wall are encountered in a variety of contexts, from large-scale applications of fully developed turbulent jets impinging on the ground, as in VTOL aircraft [1], to the small-scale use of laminar jets to determine the shear strength of vascular tissue in the study of atherogenesis [2]. Impinging jets are also used in chemical vapor deposition (CVD) processes [3,4] and in the study of laminar flames [5–9]. Work has also been done on opposed-jet stagnation flow, a configuration widely used in combustion experiments [10–13]. Definitive experimental data for laminar impinging jets in the nozzle-to-plate separation distance L to nozzle diameter d ratio (see Fig. 1) range of $0.5 \leqslant L/d \leqslant 1.5$ are not widely available. This range of L/d is useful in the study of strain-stabilized flames in combustion research. Available data in this range do not include detailed axial velocity profile measurements along the flow centerline, except for the study of Mendes-Lopes [7]. Such measurements are important in assessing one-dimensional flame models. This work focuses on the hydrodynamics of nonreacting impinging-jet flow, as a basis for related studies of strained flames [8,9].

Flow velocities in impinging jets have been measured by various means, such as laser-Doppler velocimetry (LDV) [12] or particle image velocimetry (PIV) [14]. In this study, particle streak velocimetry (PSV) [8,9,15], a technique similar to particle tracking velocimetry (PTV) [16], is used to obtain instantaneous flow-field measurements and, in particular, axial velocities along the flow centerline. A new PSV methodology has been implemented in this work that includes digital imaging, image processing, and new analysis techniques [8,9]. These improvements allow quantitative velocity data to be obtained throughout the flow field with PSV, without excessive post-processing. This allows PSV to achieve accuracies that compete favorably with LDV or PIV, while providing advantages such as low-particle-mass loading, easy discrimination against agglomerated particles that may not track the flow, short-run-time experiments, and re-

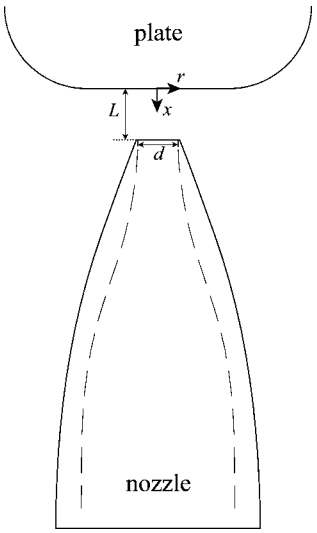

FIG. 1. Experimental geometry.

*Electronic address: jeffb@tyrvos.caltech.edu

liable velocity measurement from Lagrangian particle trajectories. The static (Bernoulli) pressure drop across the nozzle contraction is measured concurrently, providing measurement redundancy and a valuable independent parameter, as will be discussed below.

Impinging-jet flows have been described analytically, or simulated numerically, using different formulations and techniques. Schlichting [17] presents a one-dimensional axisymmetric model for an infinite-diameter jet impinging on a plate, which has been used in flame studies [5,7]. This model was extended to allow both the velocity and velocity gradient to be specified at some distance from the stagnation plate [10,18], providing a flexible boundary condition for finite-nozzle-diameter impinging-jet flows. Two-dimensional, steady, axisymmetric calculations of viscous [2] and inviscid [1,19–21] impinging-jet flow have also been performed. Except for the work of Strand [21], these calculations do not include nozzle-to-wall proximity effects.

In this work, the flow is modeled with varying levels of complexity: by means of an axisymmetric unsteady Navier-Stokes simulation, an axisymmetric potential-flow formulation, and a one-dimensional stream-function model. The first method is a spectral-element scheme [22,23] that solves the incompressible axisymmetric Navier-Stokes equations. The unsteady spectral-element method is robust and time and space accurate. The second method is a finite-difference potential-flow solution based on the classical ideal-jet approach [24,25]. The potential- and viscous-flow calculations presented here capture wall-proximity effects by including parts of the nozzle and plenum assembly in the computational domain. The one-dimensional model relies on a stream-function formulation that is used in CVD studies [3,4] and by the combustion community [5–10,18].

The experimental results are used to evaluate the accuracy of the different simulation methodologies. Additionally, new scaling parameters and empirical properties of the centerline axial velocity field are discussed. The new scaling allows the identification of an analytical expression for the axial velocity profile of a laminar impinging jet for Reynolds numbers in the range investigated of $200 \leqslant \mathrm{Re} \leqslant 1400$.

II. EXPERIMENTS

In the experiments documented here, a room-temperature jet was generated in atmospheric pressure air from a contoured nozzle with an internal (nozzle-exit) diameter of $d = 9.9$ mm. The nozzle interior was designed by optimizing the inner radius profile $r(x)$ through the contraction section, expressed in terms of a seventh-degree polynomial, to minimize the exit boundary-layer displacement thickness and avoid the formation of Taylor-Görtler vortices in the concave section (see Fig. 1 and [9]). The nozzle exterior was designed with attention to the upstream entrainment-induced flow and to avoid flow separation and unsteadiness (see Fig. 1 and [9]). The air mass flux was controlled using a sonic metering valve. The flow was seeded with particles, using a seeder developed in-house, before entering the jet plenum, where screen and honeycomb sections were used for flow uniformity and turbulence management. The nozzle-plenum system produced a uniform velocity profile in a free-jet configuration. The jet-exit velocity profile was measured with a flattened pitot probe ($d_{\mathrm{pitot}} \approx 0.4$ mm in the radial direction) and an electronic-capacitance manometer (BOC Edwards W57401100) with a temperature-stabilized 1-torr differential-pressure transducer (BOC Edwards W57011419). Figure 2 compares the nozzle-exit velocity profile with the profile obtained from the two-dimensional viscous simulation, at a Reynolds number $\mathrm{Re_j} \equiv \rho d U_\mathrm{j} / \mu \cong 1400$, where U_j is the centerline velocity at the jet exit, ρ is the density, and μ is the viscosity. The profile is uniform, with less than 1% variation outside the wall boundary layers ($r/R \leqslant 0.6$, $R = d/2$). The slight disagreement between simulation and experiment in the wall boundary layer region is attributable to the finite pitot-probe extent in the radial direction d_{pitot}, for which no corrections were applied.

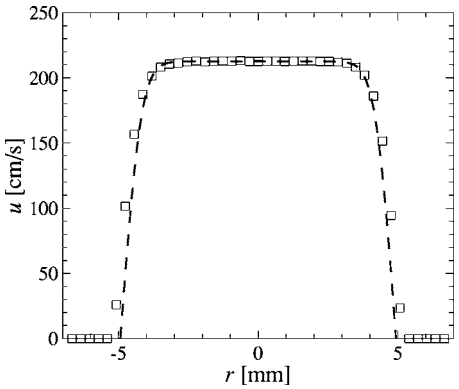

FIG. 2. Nozzle-exit velocity profile ($d = 9.9$ mm, $\mathrm{Re_j} = 1400$): (□) experimental data, (dashed line) viscous-simulation results. Pitot-probe internal opening is $d_{\mathrm{pitot}} \approx 0.4$ mm.

The jet was aligned normal to a solid wall (stagnation plate assembly), at separation-distance to nozzle-diameter ratios of $L/d = 0.7$, 1.0, and 1.4. Significant changes in flow characteristics are observed over this L/d range. The stagnation plate was a circular, copper block, 7.62 cm (3 in.) in diameter and 5.08 cm (2 in.) thick, with a 2.03-cm (0.8-in.) bottom-edge radius. A bottom-edge radius was introduced to mitigate upstream effects of flow-separation and edge-flow unsteadiness in the stagnation-flow region (see Fig. 1).

PSV is well suited as a velocity-field diagnostic for this flow. In this axisymmetric, steady flow, the axial velocity component can be reliably measured on the centerline. Particle paths do not cross or overlap, and out-of-plane particle displacements are small and easily discernible when they occur (in-focus and out-of-focus streaks). The high sensitivity of the scattering cross section to particle size, in the size range employed, allows easy identification of agglomerates that may not track the high-spatial-gradient regions in the flow. Streaks used for PSV processing were from in-plane, nonagglomerated particles. A single image frame can capture the entire velocity field, allowing PSV to be implemented in short-run-time experiments. A sample image of a cold-jet flow with particle streaks is reproduced in Fig. 3, for a nozzle-to-plate separation distance to nozzle-diameter ratio of $L/d = 1.0$. In this flow, the jet-nozzle centerline velocity is $U_\mathrm{j} = 106$ cm/s, yielding a Reynolds number $\mathrm{Re_j} \cong 700$. The

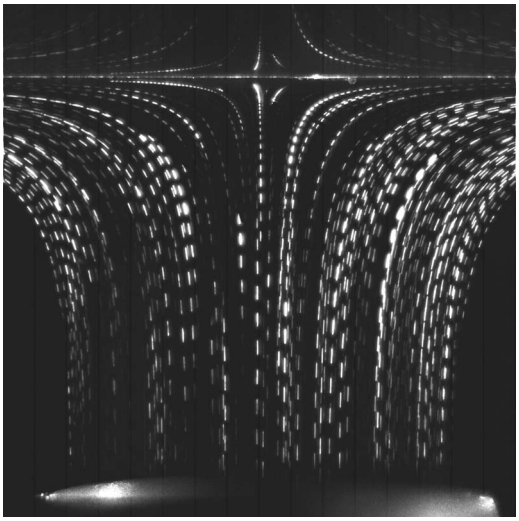

FIG. 3. Impinging-jet flow ($\mathrm{Re_j}=700$, $U_j=106$ cm/s, $L/d=1.0$). Stagnation plate and nozzle exit are visible. The nozzle-exit diameter is $d=0.99$ cm. The image width corresponds to ≈ 1.2 cm.

top and bottom portions of the laser sheet are masked to minimize scattering from the solid plate and nozzle surfaces.

In a variable-velocity field, particles will follow the flow if the dimensionless product of the local strain rate $\sigma = \mathrm{d}u/\mathrm{d}x$ and the Stokes time τ_S is small—i.e., if,

$$\sigma\tau_S \equiv \sigma\frac{\rho_p d_p^2}{18\mu} \ll 1. \tag{1}$$

Measurements relied on alumina particles (Al_2O_3; median size, $d_p \cong 0.8$ μm, $\rho_p \cong 3830$ kg/m^3; Baikowski Malakoff, RC-SPT DBM). At the maximum strain rates encountered in these experiments, $\sigma\tau_S \cong 3\times 10^{-3}$.

A Coherent I-90 Ar-ion (CW) laser, operated at 2–3 W, was the illumination source. Two cylindrical lenses generated a thin laser sheet (≈ 500 μm) in the field of view. An Oriel chopper system (model 75155), with a 50% duty-cycle wheel, modulated the laser beam. The chopper was placed at a horizontal waist in the laser beam to minimize chopping (on-off and off-on transition) times. Chopping frequencies were in the range $0.5\ \mathrm{kHz} \leqslant \nu_c \leqslant 2.4\ \mathrm{kHz}$, with ν_c optimized depending on flow velocity, in each case.

Image data were recorded with the in-house-developed "Cassini" and "KFS" digital-imaging systems (see [9]). They are based on low-noise, 1024^2-pixel charge-coupled devices (CCDs), on a 12-μm pitch. The Cassini camera is based on a CCD developed for the NASA Cassini mission. The KFS CCD was designed by M. Wadsworth and S. A. Collins of JPL. The camera heads and data-acquisition systems were designed and built by D. Lang at Caltech. Output for both is digitized to 12 bits/pixel. Magnification ratios were in the range of 1:1-1:1.5, using a Nikon 105-mm, $f/2.8$ macro lens. Exposure times were varied for optimum particle-streak density in the images, with framing rates for these experiments in the range of 8–10 fps.

Small-particle streaks approximate Lagrangian trajectories of the flow (see Fig. 3). Local velocities $u(x)$ are estimated from streak pairs as $u(x) \cong \Delta X(x)/\Delta t$, yielding $u_I = L_I/\tau_c$ and $u_{II} = L_{II}/\tau_c$, where $\tau_c = 1/\nu_c$ (reciprocal of chopper frequency) and $L_I = x_{2s} - x_{1s}$ and $L_{II} = x_{2e} - x_{1e}$ are the distances from the start or end of one streak to the start or end of the next, respectively (see Fig. 4). The velocity estimate u_I is located at $x_I = (x_{1s} + x_{2s})/2 + (w_1 + w_2)/4$, where x_{is} is the spatial location of the start of the ith streak and w_i is the width of the ith streak (see Fig. 4). Similarly, u_{II} is located at $x_{II} = (x_{1e} + x_{2e})/2 - (w_1 + w_2)/4$, where x_{ie} is the location of the end of the ith streak. Using the same intensity threshold on a streak pair removes systematic errors in applying the Lagrangian time interval τ_c. This methodology produces good agreement between velocity values derived from each streak pair. Streak lengths are estimated using bicubic fits on the two-dimensional streak-intensity image data, sampled to a 0.1-pixel resolution in both dimensions. An intensity threshold of approximately 0.4 of the maximum intensity of each streak is used to determine streak dimensions to this sampling resolution. The results are not sensitive to this choice and yield an overall PSV error of $< 0.01 U_B$.

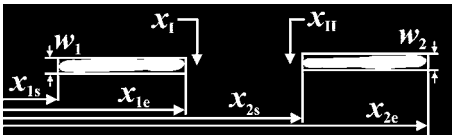

FIG. 4. PSV measurement implementation. The image width corresponds to ≈ 1 mm.

The (Bernoulli) pressure difference between the jet plenum interior, at the straight section upstream of any contraction-section curvature, and the static pressure close to, but outside the jet-core flow region, was measured with an electronic-capacitance manometer (BOC Edwards W57401100) and a temperature-stabilized, 1-torr full-scale, differential-pressure transducer (BOC Edwards W57011419). Bernoulli and mass-flow data were acquired using the National Instruments LabView hardware-software environment, synchronized to the digital-image acquisition to provide independent concurrent estimates of jet-exit velocity for every image. The Bernoulli velocity

$$U_B = \sqrt{\frac{2\Delta p/\rho}{1-(d/d_p)^4}} \tag{2}$$

was then calculated, where Δp is the static pressure drop across the nozzle, ρ is the density of the jet fluid (air), d is the diameter of the nozzle exit, and d_P is the plenum diameter. At the flow velocities in this study, Bernoulli pressure differences were in the range of 0.1–3 Pa. At the lowest speeds investigated, an error of $< 0.01 U_B$ required an absolute measurement accuracy for the Bernoulli pressure drop of $\delta(\Delta p) \leqslant 2\times 10^{-3}$ Pa $= 2\times 10^{-8}$ bar. This accuracy is achievable with the differential-pressure transducer employed if instrumental drifts and offsets are monitored. The Bernoulli pressure drop cannot be used to determine the jet-exit velocity for $L/d \leqslant 1$ because streamline curvature in the nozzle-exit plane produces a velocity deficit at the centerline [11]. However, the Bernoulli pressure drop is an important parameter for this flow, as discussed below. Mass flow rate was

also measured concurrently (Omega FMA872-V-Air), providing an independent velocity estimate.

III. NUMERICAL SIMULATIONS

In this study, three different numerical simulations were performed at varying levels of complexity. The first is an axisymmetric viscous Navier-Stokes simulation, the second is a potential-flow calculation, and the third is a one-dimensional stream-function formulation.

A. Axisymmetric Navier-Stokes formulation

The first numerical study relies on a spectral-element method [26] in an axisymmetric domain. The simulation code was developed by the authors and integrates the axisymmetric Navier-Stokes equations, with boundary conditions specified to capture this flow. Only a limited number of studies have employed the spectral-element method to study this type of flow. Frouzakis *et al.* [13] utilized the spectral-element method to study the flow field of opposed jets and flames, similar to the impinging-jet flows studied here. In that work, velocity boundary conditions were prescribed at the nozzle-exit locations. In this study, the inclusion of the nozzle interior and exterior allows nozzle-to-wall proximity effects, as well as entrainment, to be investigated.

The spectral-element method is a class of finite-element methods that can handle complex geometries. Additionally, this technique can achieve spectral accuracy by approximating the solution on Gauss-Lobatto-Legendre collocation points within each element. For elements adjacent to the axis, special Gauss-Radau-Legendre collocation points with a quadratic argument are utilized to achieve the appropriate parity for each field [27]. The code integrates a nondimensional form of the unsteady, incompressible, Navier-Stokes equations

$$\nabla \cdot \mathbf{u} = 0, \tag{3a}$$

$$\frac{\partial \mathbf{u}}{\partial t} = \mathbf{N}(\mathbf{u}) + \frac{1}{\mathrm{Re}}\mathbf{L}(\mathbf{u}) - \nabla p, \tag{3b}$$

where the nonlinear term $\mathbf{N}(\mathbf{u}) = -1/2[\mathbf{u}\cdot\nabla\mathbf{u} + \nabla\cdot(\mathbf{uu})]$ is cast into the skew-symmetric form to reduce aliasing errors. The linear diffusion term is $\mathbf{L}(\mathbf{u}) = \nabla^2\mathbf{u}$.

Figure 5 shows the elements and boundary conditions used for $L/d = 1.424$. In the current simulations, 9th- to 15th-order polynomials are used in each element. These choices provide a balance between desired solution accuracy and reasonable computational time. These boundary conditions reasonably model the experimental apparatus used in this study. The unsteady Navier-Stokes equations are integrated in time until the solution attains a steady-state condition, starting with the flow at rest in the domain interior.

A study of the effects of boundary conditions on the flow field was undertaken to ascertain that the near-field solution was insensitive to the particular choices. A nearly flat velocity profile is introduced at the nozzle inlet (Fig. 5), $u_1(r)/U_\mathrm{P} = -\tanh[c_1(1 - r/r_\mathrm{P})]$, where $r_\mathrm{P} = d_\mathrm{P}/2$ is the radius of the plenum, U_P is the centerline velocity at the plenum,

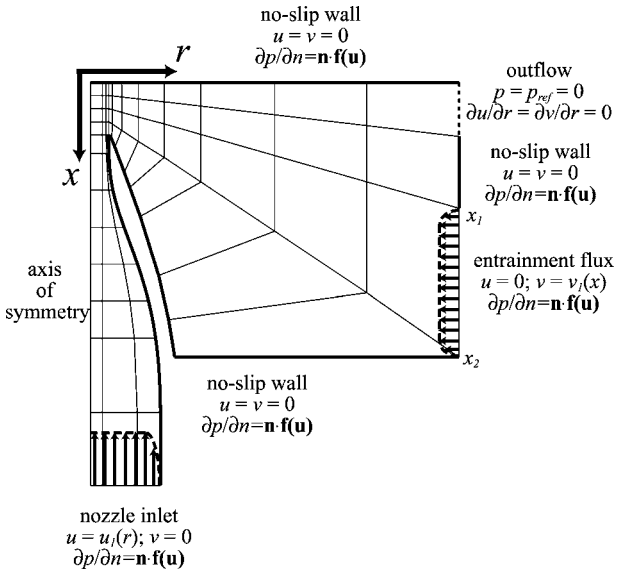

FIG. 5. Axisymmetric Navier-Stokes simulation domain and boundary conditions. $\mathbf{f}(\mathbf{u}) = \nabla p = \mathbf{N}(\mathbf{u}) + \mathbf{L}(\mathbf{u})/\mathrm{Re}$. $u_1(r)$ and $v_1(x)$ are the nozzle and entrainment inlet velocity profiles, respectively.

and c_1 was set to 50. This profile mimics the outflow from the turbulence-management section in the experiments. As expected, the jet profile at the nozzle exit is insensitive to the choice of inlet profile, owing to the high contraction ratio in the nozzle design (see Fig. 1).

To simulate the entrained flow, an entrainment flux Q_e is introduced through the lower portion of the outer boundary. Over the range $1/4 \leq Q_e/Q \leq 4$, where $Q = 2\pi\int_0^{r_\mathrm{P}} r u_1(r)\mathrm{d}r$ is the mass flux through the nozzle, the maximum difference in the velocity field was $0.008U_\mathrm{B}$ in the near-field region of interest ($0 \leq r/d \leq 1$, $0 \leq x/d \leq L/d$). For the entrainment flux (bottom right), $v_1(x)/U_\mathrm{P} = -c_2 \tanh[c_3(x - x_1)(x_2 - x)/(x_2 - x_1)^2]$ is specified (Fig. 5), with $c_2 = 0.0785$ and $c_3 = 50$. These choices yield $Q_\mathrm{e}/Q \approx 1.8$. A uniform-pressure condition is specified near the wall at the boundary of the domain exhaust, marked "outflow" in Fig. 5.

B. Potential-flow formulation

For axisymmetric flow, the continuity equation can be satisfied by expressing the velocity field in terms of a stream function, $\psi(x, r)$—i.e.,

$$u = \frac{1}{r}\frac{\partial \psi}{\partial r}, \quad v = -\frac{1}{r}\frac{\partial \psi}{\partial x}. \tag{4}$$

In the absence of swirl, the azimuthal vorticity ω is related to the stream function by (e.g., Batchelor [28])

$$-r\omega = \frac{\partial^2 \psi}{\partial x^2} + \frac{\partial^2 \psi}{\partial r^2} - \frac{1}{r}\frac{\partial \psi}{\partial r} = r^2 \frac{\mathrm{d}H}{\mathrm{d}\psi}, \tag{5}$$

where $H(\psi)$ is the Bernoulli constant,

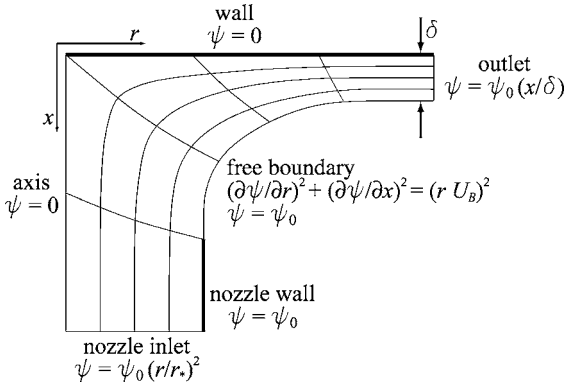

FIG. 6. Potential-flow simulation domain and boundary conditions.

$$H(\psi) \equiv \frac{1}{2}(u^2 + v^2) + \frac{p}{\rho}. \tag{6}$$

One approach to the inviscid impinging-jet problem is to specify an inlet axial velocity profile at some distance from the wall, determine $H(\psi)$ at that location, and then solve Eq. (5) in a domain bounded by the axis of the jet, the wall, and specified inlet and outlet boundaries [1]. This approach is satisfactory provided the inlet conditions are not affected by the jet impingement.

In this study, we follow the conventional ideal-jet approach [24,25], where the interior flow is irrotational, the shear layers are infinitesimally thick, and the exterior flow is stagnant. Setting the right-hand side of Eq. (5) to zero, the equation for the stream function in the jet interior is then

$$\frac{\partial^2\psi}{\partial x^2} + \frac{\partial^2\psi}{\partial r^2} - \frac{1}{r}\frac{\partial\psi}{\partial r} = 0. \tag{7}$$

The surface of the jet is a streamline; hence, $\psi(x_0, r_0) = \psi_0$, where ψ_0 is a constant and (x_0, r_0) are coordinates of any point on the surface of the jet. The location of the jet surface, (x_0, r_0), is not known *a priori* and must be determined as part of the solution to satisfy the constant-pressure boundary condition

$$u^2 + v^2 = \frac{1}{r^2}\left[\left(\frac{\partial\psi}{\partial x}\right)^2 + \left(\frac{\partial\psi}{\partial r}\right)^2\right] = U_B^2, \tag{8}$$

where U_B is the Bernoulli velocity. Schach [20] solved this problem using an integral equation approach, assuming the nozzle outflow was not affected by proximity to the wall. Strand [21] used a truncated series solution (up to four terms) to solve for two cases: $L/d \geqslant 1$ (ignoring wall-proximity effects) and $L/d \ll 1$. This approach, however, omits the transitional regime $0.5 \leqslant L/d \leqslant 1.5$ of interest in this study.

The physical domain and boundary conditions are summarized in Fig. 6. Equation (7) was discretized using second-order centered finite differences on a fixed rectangular computational domain. This domain was mapped to the physical domain by the solution of two elliptic partial differential equations for the physical coordinates x and r. These equations were coupled to Eq. (7) through the boundary condition of Eq. (8). The simultaneous solution of these equations determines the shape of the free constant-pressure boundary. To capture wall-proximity effects, a constant-diameter nozzle is included in the computational domain. Instead of prescribing the nozzle radius, a finite-velocity constraint is applied at the trailing edge of the nozzle. Uniform axial and radial velocity profiles were prescribed at the inlet and outlet of the domain, respectively. The inlet and outlet were positioned about four and eight nozzle radii from the wall stagnation point, respectively.

Second-order accuracy was verified by solving for infinite stagnation-point flow on grids generated from the solution of the impinging-jet problem at resolutions ranging from 20×80 to 80×320. The analogous plane-flow impinging-jet problem was also solved and compared to the analytic solution outlined by Birkhoff and Zarantonello [24]. The error in the discharge coefficient was less than 1% with excellent agreement between the numerical and analytic free boundaries. For the axisymmetric impinging-jet problem, convergence studies were conducted at resolutions ranging from 20×80 to 80×320. Differences in the centerline axial velocity were less than $0.01 U_B$. Sensitivity to the radial extent of the domain was studied by reducing the outlet radius to four nozzle radii. The difference in the centerline axial velocity was, again, less than $0.01 U_B$. The gradient of the centerline axial velocity decayed to almost zero at the nozzle inlet, indicating that the inlet was placed sufficiently far from the wall.

C. Stream-function formulation

The one-dimensional solution for constant-density stagnation flows models the flow in terms of a local stream function $\psi(x,r) = r^2 U(x)/2$, which leads to $u(x) = U(x)$ and $v(x,r) = -rU'(x)/2$ [see Eq. (4)]. The axisymmetric Navier-Stokes equations can then be expressed in terms of the axial velocity, $U(x)$—i.e.,

$$\nu U''' - UU'' + \frac{1}{2}U'^2 = -\frac{2\Lambda}{\rho}, \tag{9}$$

where Λ is termed the radial-pressure eigenvalue of the problem,

$$\Lambda = \frac{1}{r}\frac{\partial p}{\partial r}, \tag{10}$$

which, in this formulation, must be a constant. Appendix A provides further discussion on the spatial variation in Λ. The third-order ordinary differential equation requires three boundary conditions at $x = 0$. It is common to specify boundary conditions at $x = 0$ and $x = \ell$ with $0 < \ell \leqslant L$ some interior point, by adjusting the curvature boundary condition at $x = 0$ to achieve the desired boundary condition at $x = \ell$. A fourth boundary condition can be satisfied by adjusting Λ,

$$U(0) = 0,$$

$$U'(0) = 0,$$

$$U(\ell) = -U_\ell,$$

$$U'(\ell) = -U'_\ell, \tag{11}$$

Since $u(\ell, r) < 0$ (flow is towards the stagnation plate), the negative signs are chosen for convenience to make the constants U_ℓ and U'_ℓ positive. Plug-flow boundary conditions—i.e., $U'(\ell)=0$—at the nozzle exit plane, $\ell = L$, are commonly specified with this formulation. The inviscid outer solution to Eq. (9) is a parabola. In the inviscid limit, the flow is irrotational if $\Lambda = -\rho(U'_\ell)^2/4$, for which the solution reduces to potential stagnation flow where the coefficient of the curvature term is identically zero—i.e., linear outer flow, $U'_\ell = U_\ell/\ell$. For more general boundary conditions, the resulting flow has vorticity, whereas the core of the experimental jet is irrotational. The introduction of vorticity to the flow is necessary to accommodate outer flows with curvature. The equations are solved using the CANTERA software package [4].

IV. RESULTS AND DISCUSSION

The experimental velocity data reported here were recorded at three nominal Reynolds numbers

$$\mathrm{Re} \equiv \frac{\rho d U_\mathrm{B}}{\mu} \cong 400,\ 700,\ \text{and}\ 1400, \tag{12}$$

with actual values within ±35, in each case, and at three nozzle-to-stagnation plate separation distance to nozzle-exit-diameter ratios $L/d \cong 0.7$, 1.0, and 1.4. Figure 7 compares measured axial velocities, scaled by the Bernoulli velocity, for the three L/d ratios at the three Reynolds numbers. The velocity profiles collapse to a single curve, independent of L/d, if the axial velocity is scaled by the Bernoulli velocity. A centerline axial velocity deficit at the jet exit develops as the separation distance is decreased due to the influence of the stagnation point on the nozzle flow [11]. Notably, the velocity and its gradient adjust to maintain self-similarity, with the Bernoulli velocity scaling the flow.

Figure 8 shows the axisymmetric viscous simulation results at Re=700 and variable L/d. The velocity profiles follow a single curve when velocities are scaled by the Bernoulli velocity, consistent with the experimental results. Figure 9 gives pressure contours at $L/d=0.5$ and 1.4, with pressures scaled by the Bernoulli pressure. The near-wall pressure field is not significantly altered by changes in the nozzle position. As the separation distance is reduced, the stagnation-point pressure field extends into the nozzle, altering the nozzle flow. Figure 10 compares the experimental data with the axisymmetric viscous calculations at $L/d=1.4$ and Re=400, 700, and 1400. The inset of Fig. 10 shows the residuals between the simulated, u_sim, and measured, u_PSV, velocities, normalized by the Bernoulli velocity U_B. The differences between experimental and numerical results for these three cases are less than $0.015U_\mathrm{B}$ root mean squared (rms), indicating that the experimental flow field is adequately modeled. Figure 11 compares particle-streak-image data and streamlines from the axisymmetric viscous simulations. Good qualitative agreement can be seen, even in the entrainment region where the velocities are low ($<0.02U_\mathrm{B}$).

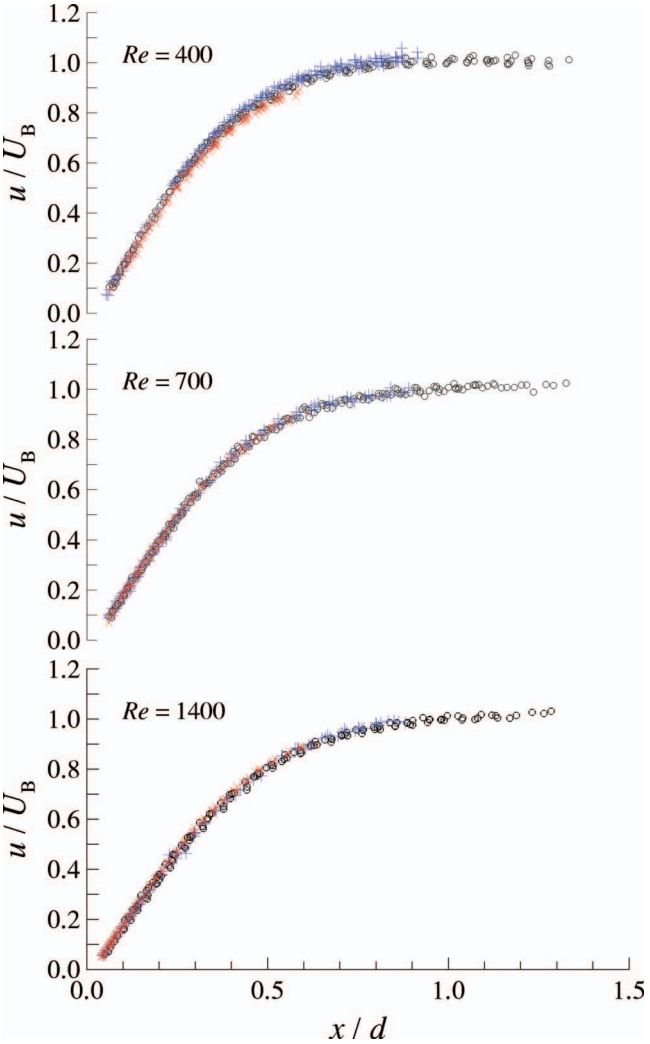

FIG. 7. (Color) Comparison of velocity versus axial distance from plate at three nominal Reynolds numbers. Velocities are scaled by the Bernoulli velocity and axial distances by the nozzle diameter. Experimental results for separation distances of $L/d=0.7(\times)$, $L/d=1.0(+)$, and $L/d=1.4(\bigcirc)$.

Figure 12 compares the experimental data at the highest Reynolds number to the potential-flow results, with the normalized residuals between simulation and experiment plotted in the inset. Here the axial distance is normalized by the effective diameter d_*, where d_* is the nozzle diameter corrected for the nozzle-wall boundary-layer displacement thickness. One of the main effects of the Reynolds number in this flow is the change in the effective jet diameter through the boundary-layer displacement thickness. This effect should be removed before comparing the experiments to the inviscid potential-flow results, which are valid in the limit of infinite Reynolds number. The boundary-layer thicknesses are estimated from axisymmetric, viscous simulations of the nozzle flow. The small disagreement close to the wall is attributable to wall boundary-layer displacement effects. This discrepancy leads to a difference in the maximum centerline axial velocity gradient. As with the experimental results, the axial velocity profiles collapse independent of L/d.

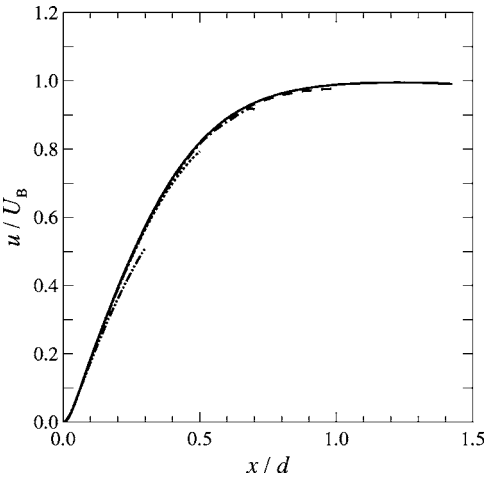

FIG. 8. Scaled velocity versus axial distance from plate. Viscous calculations at Re=700 and L/d=0.3 (dash–double-dotted line), 0.5 (dotted line), 0.7 (dash-dotted line), 1.0 (dashed line), and 1.4 (solid line).

Figure 13 compares the experimental axial velocity data, at Re=700, to four different one-dimensional simulations, with plug-flow boundary conditions and different choices of the interior boundary location ℓ. Plug-flow boundary conditions capture the flow only for ℓ/d=0.8. This is due to the fact that the outer solution to the one-dimensional equations is a parabola and cannot capture the free-jet behavior (zero-gradient region of flow) that is exhibited for $x/d>1.0$. Finite-velocity gradients are evident for $x/d<0.8$. The value of ℓ/d=0.8 is an intermediate case for which plug-flow boundary conditions capture the flow. The approximations invoked in arriving at the one-dimensional stream-function model are valid in the limit of an infinite-diameter jet impinging on a surface. However, from Fig. 13 it appears that the model should be able to capture the flow in the region $0 \leqslant x/d<0.8$ if appropriate boundary conditions are specified. The velocity and velocity-gradient boundary conditions at a given axial location, $U(\ell)$ and $U'(\ell)$, can be specified from an error-function fit to the experimental data [see Eq. (13)]. The one-dimensional solution calculated using this

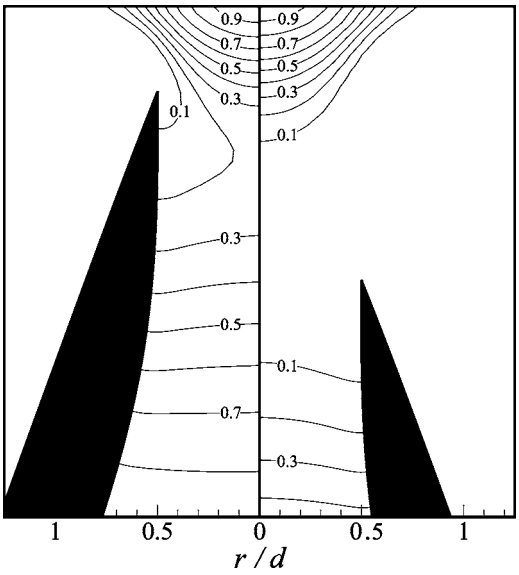

FIG. 9. Pressure contours, normalized by the Bernoulli pressure, at L/d=0.5 (left) and L/d=1.4 (right).

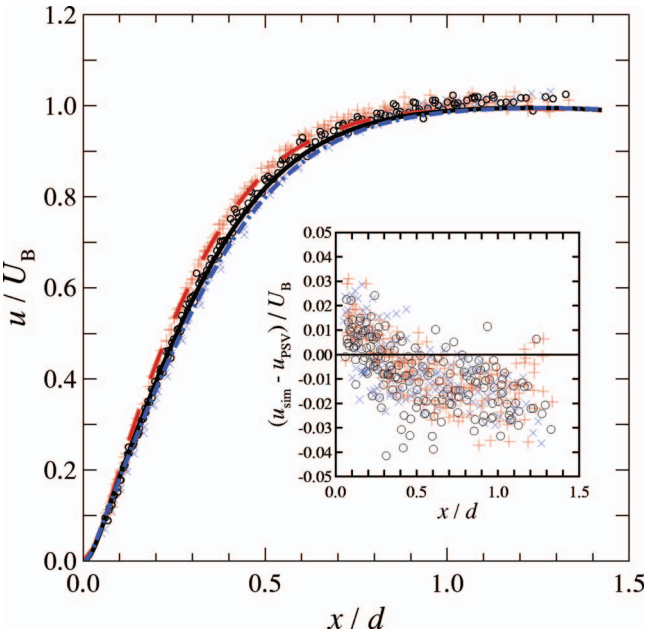

FIG. 10. (Color) Scaled velocity versus axial distance from plate. Viscous calculations (lines) and experimental data (symbols) at Re=400 (dashed line, +), 700 (solid line, ○), and 1400 (dash-dotted line, ×). The inset shows the residuals between the simulated, u_{sim}, and measured, u_{PSV}, velocities, normalized by the Bernoulli velocity U_B. Symbols and colors correspond to the Re of the main plot.

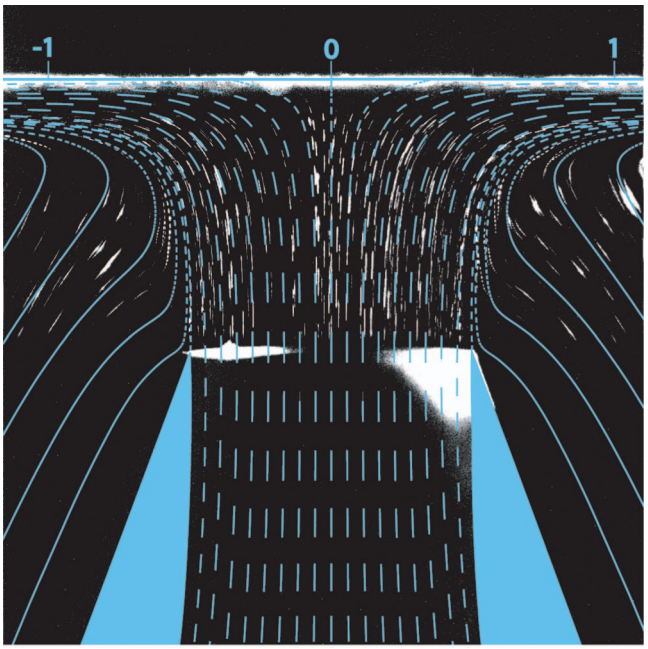

FIG. 11. (Color) Particle streak image (monochrome) detailing entrained flow with superimposed axisymmetric viscous calculation (blue lines) at Re=700 and L/d=1.0.

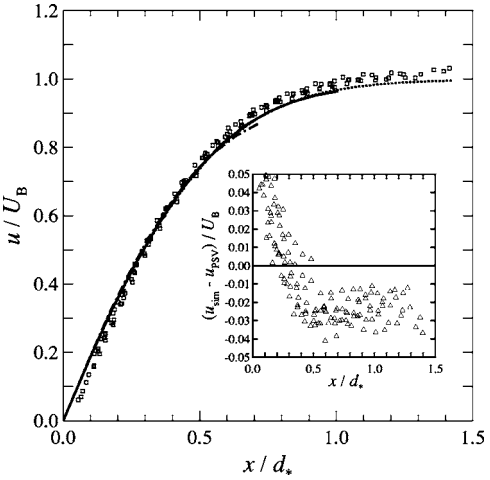

FIG. 12. Scaled velocity versus axial distance from plate normalized by the effective diameter d_*. Experimental data at Re $=1400$ (□) and potential-flow simulations (lines) at $L/d_*=0.7$ (dash-dotted line), $L/d_*=1.0$ (solid line), and $L/d_*=1.4$ (dotted line). The inset shows the residuals between the simulated, u_{sim}, and measured, u_{PSV}, velocities, normalized by the Bernoulli velocity U_{B}.

method at Re$=700$, over the range $0.3 \leqslant \ell/d \leqslant 0.7$, has a maximum error of less than $0.03U_{\mathrm{B}}$ when compared to axisymmetric viscous simulations. Figure 14 shows the one-dimensional simulation results compared to experimental data at Re$=700$, with boundary conditions taken from the experimental data at $\ell/d=0.6$. The normalized residuals between simulation and experiment are plotted as an inset.

In their study of turbulent jets, Kostiuk *et al.* [12] showed that opposed- or impinging-jet velocity data are well characterized by an error function and used the parameters obtained from the error-function fit to collapse their experimental data. Their error function contained three adjustable parameters: the velocity at infinity U_∞, a strain-rate parameter α, and a wall-offset length δ/d,

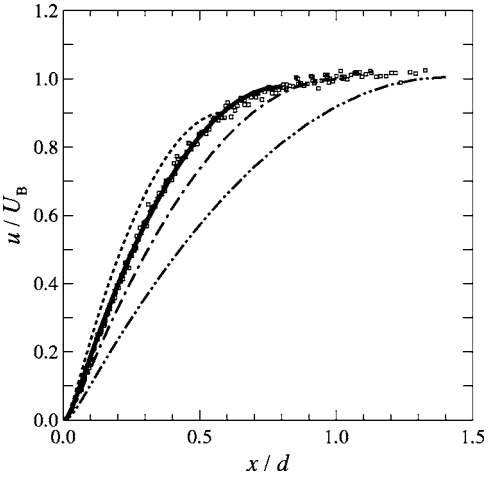

FIG. 13. Comparison of one-dimensional stream-function simulations with plug-flow boundary conditions (lines) to experimental results (□) at Re$=700$, varying ℓ: $\ell/d=0.6$ (dashed line), $\ell/d=0.8$ (solid line), $\ell/d=1.0$ (dash-dotted line), and $\ell/d=1.4$ (dash–double-dotted line).

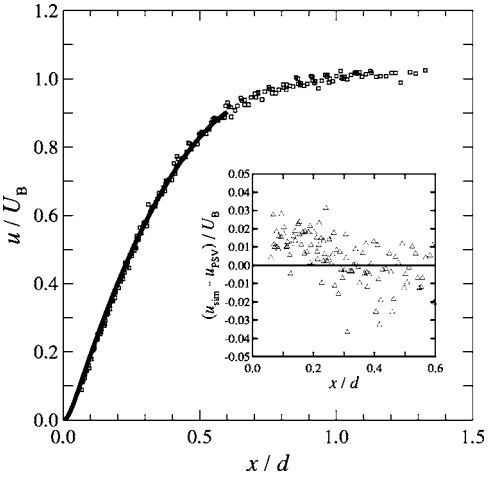

FIG. 14. Comparison of one-dimensional stream-function simulation (line) to experimental data (□) at Re$=700$. Boundary conditions calculated from error-function fit to the data at $\ell/d=0.6$. The inset shows the residuals between the simulated, u_{sim}, and measured, u_{PSV}, velocities normalized by the Bernoulli velocity U_{B}.

$$\frac{u(x)}{U_\infty} = \mathrm{erf}\left[\alpha\left(\frac{x}{d} - \frac{\delta}{d}\right)\right]. \tag{13}$$

The collapse of the experimental and numerical data discussed above suggests that the appropriate velocity scale for laminar impinging jets is the Bernoulli velocity—i.e., $U_\infty = U_{\mathrm{B}}$. From one-dimensional viscous stagnation-flow theory (see Appendix B), the scaled-offset length δ/d, which is proportional to the scaled wall boundary-layer thickness, can be related to the strain-rate parameter α, such that

$$\frac{\delta}{d}(\mathrm{Re}, \alpha) = 0.755\sqrt{\frac{1}{\mathrm{Re}\ \alpha}}. \tag{14}$$

Thus, the only free parameter in this error-function fit to the data is the strain-rate parameter α, which should be a func-

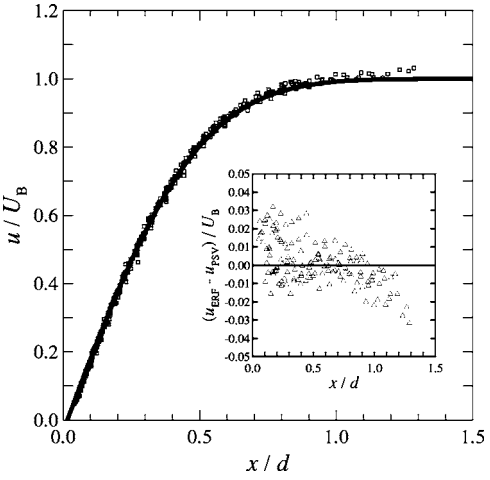

FIG. 15. Comparison of error-function fit (line) to experimental data (□) at Re$=1400$. The inset shows the residuals between the error function, u_{ERF}, and measured, u_{PSV}, velocities, normalized by the Bernoulli velocity U_{B}.

TABLE I. Error-function fit parameters and rms error ϵ_{rms} of fits to experimental and viscous-simulation data.

Re	α	δ/d	Experiment $\epsilon_{\mathrm{rms}}/U_{\mathrm{B}}$	Simulation $\epsilon_{\mathrm{rms}}/U_{\mathrm{B}}$
400	2.21	0.027	0.017	0.014
700	2.00	0.020	0.010	0.009
1400	1.88	0.015	0.011	0.010

tion of Reynolds number alone—i.e., $\alpha=\alpha(\mathrm{Re})$. Therefore, the axial velocity field for an axisymmetric impinging laminar jet is fully specified by the Bernoulli velocity U_{B}, since the Reynolds number is, in turn, derived from it.

The error-function fit to the data at Re=1400 is plotted in Fig. 15, with the normalized residuals between the error function and experiment shown in the inset. The error function was fit to each experimental and viscous simulation case by adjusting α such that the root-mean-squared (rms) error was minimized. For each Reynolds number, the strain-rate parameter α was averaged over the range $0.7\leqslant L/d\leqslant 1.4$. This single $\alpha(\mathrm{Re})$ dependence was subsequently used in all error-function fits to determine the resulting rms error ϵ_{rms}. The fit parameters and ϵ_{rms} are shown in Table I. The strain-rate parameter is found to scale with Reynolds numbers as $\alpha=\alpha_\infty+C_1/\mathrm{Re}$, with the constants $\alpha_\infty=1.775$ and $C_1=153$ determined by fitting the $\alpha(\mathrm{Re})$ values in Table I.

As previously mentioned, the main Reynolds number effect for this flow is through the nozzle-wall boundary-layer thickness. The effect of the nozzle-exit velocity profile is studied in Fig. 16 for profiles varying from a top-hat shape, representative of the outflow from a high-contraction ratio nozzle, to a parabolic profile, representative of laminar pipe flow. Real nozzle-exit velocity profiles will lie in between these two extremes (see Fig. 2). Intermediate cases are studied by specifying hyperbolic tangent profiles whose coefficients are adjusted to obtain a variation of boundary-layer displacement thicknesses. The results in Figs. 16 and 17 are obtained by removing the nozzle interior from the axisymmetric-viscous-simulation domain and specifying the velocity profiles at the nozzle exit. Due to the lack of a plenum in the simulations, velocities are scaled by the velocity at the axis of the jet U_{j}, instead of the Bernoulli velocity. Figure 16 indicates that there is a significant effect of the nozzle-exit velocity profile on the resultant axial velocity field. Figure 17 plots the axial velocity profiles with the axial distance normalized by the boundary-layer thickness corrected diameter d_*. For $d_*/d>0.9$ this scaling results in a good collapse of the profiles.

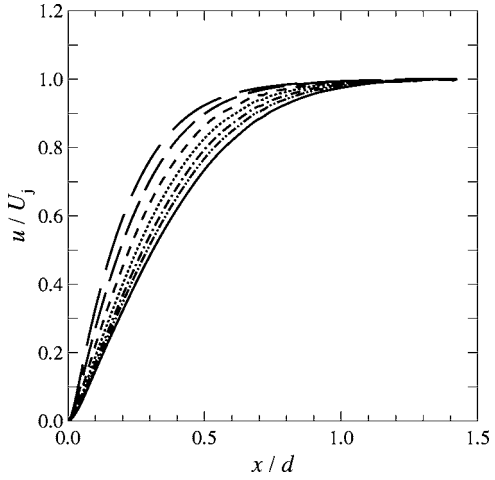

FIG. 16. Simulated velocity profiles at Re=700 and $L/d=1.4$ for variable nozzle-exit velocity profiles: parabolic ($d_*/d=0.71$, long-dashed line), hyperbolic-tangent profiles with $d_*/d=0.76$ (medium-dashed line), $d_*/d=0.82$ (dashed line), $d_*/d=0.87$ (dotted line), $d_*/d=0.91$ (dash-dotted line), $d_*/d=0.95$ (dash–double-dotted line), and top-hat ($d_*/d=1.0$, solid line) profiles.

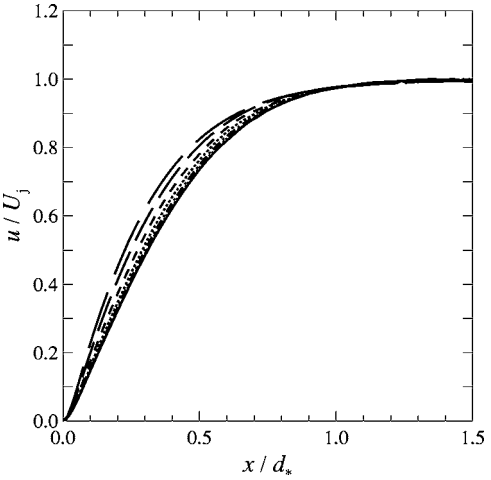

FIG. 17. Simulated velocity profiles versus axial distance from plate normalized by the effective diameter d_* at Re=700 and $L/d=1.4$ for variable nozzle-exit velocity profiles. Legend as in Fig. 16.

From the previous results, the displacement-thickness-corrected diameter d_* is an appropriate scaling parameter for axial distances. Figure 18 shows the scaled velocity profiles from axisymmetric viscous simulations at four Reynolds numbers. For low Reynolds numbers (Re=200) viscous

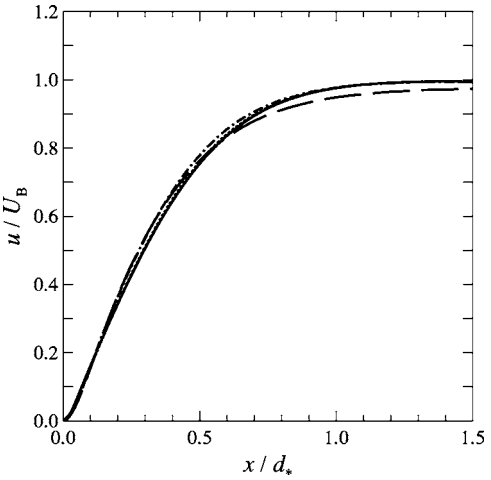

FIG. 18. Axisymmetric viscous simulation velocity profiles versus axial distance from plate normalized by the effective diameter d_* at $L/d=1.4$ and Re=200 (long-dashed line), 400 (dash-dotted line), 700 (dotted line), and 1400 (solid line).

losses result in a jet-exit velocity that is less than the Bernoulli velocity. There is an additional weak Reynolds number effect exhibited for Re=200 and 400 that is not fully captured by the current scaling and is manifested in the slope of the profiles. However, the velocity profiles collapse reasonably well using this scaling, and this allows the specification of an analytical expression for the velocity profile of the impinging jet in this Reynolds number range,

$$\frac{u(x)}{U_{\mathrm{B}}} = \mathrm{erf}\left[\alpha_*\left(\frac{x}{d_*} - \frac{\delta}{d_*}\right)\right], \tag{15}$$

where $\alpha_*=1.7$ and $\delta/d_*=0.016$ were found from fitting this error function to the axisymmetric-viscous-simulation data. The rms error of the error-function fit is less than 0.5% for Re=700 and 1400 and less than 2% for Re=200 and 400. In the limit of infinite Reynolds number, the wall boundary-layer thickness will tend to zero and the potential flow formulation will accurately model the flow. In this limit, the velocity field is given by $u/U_{\mathrm{B}}=\mathrm{erf}[\alpha_{\mathrm{p}}(x/d_*)]$, with $\alpha_{\mathrm{p}}=1.59$ found by fitting this error function to the potential flow simulations. These expressions yield the velocity profile for an impinging jet with a measurement of the Bernoulli pressure across the nozzle contraction, the gas density and viscosity, the diameter ratio of the nozzle inlet and outlet, and the boundary-layer thickness at the nozzle exit.

V. CONCLUSIONS

Scaling the centerline axial velocity for an impinging jet by the Bernoulli velocity, calculated from the static pressure drop across the nozzle contraction, collapses centerline axial-velocity data on a single curve that is independent of the nozzle-to-plate separation distance for separation-to-diameter ratios of $L/d \geqslant 0.5$. The axisymmetric viscous and potential-flow simulations reported here allow nozzle-to-wall proximity effects to be investigated by including the nozzle in the solution domain. Using this simulation domain, axisymmetric viscous simulations yield good agreement with experiment and confirm the velocity profile scaling. The potential-flow simulations reproduce the collapse of the data; however, at these Reynolds numbers, viscous effects result in disagreement with experiment. One-dimensional stream-function simulations provide an adequate approximation of the flow in the stagnation region if the boundary conditions are correctly specified.

The scaled axial velocity profiles are well characterized by an error function with one Reynolds-number-dependent parameter α. The error function provides a good fit to both experimental and viscous-simulation data, with root-mean-squared errors of $\epsilon_{\mathrm{rms}} \lesssim 0.02 U_{\mathrm{B}}$. In this Reynolds number range, viscous effects are captured by scaling the axial distance by the effective (displacement-thickness-corrected) diameter d_*. This scaling relies on thin nozzle boundary layers (d_*/d close to unity) and negligible viscous losses through the nozzle. These scalings allow the specification of an analytical expression for the velocity profile of an impinging laminar jet over the Reynolds number range investigated of $200 \leqslant \mathrm{Re} \leqslant 1400$.

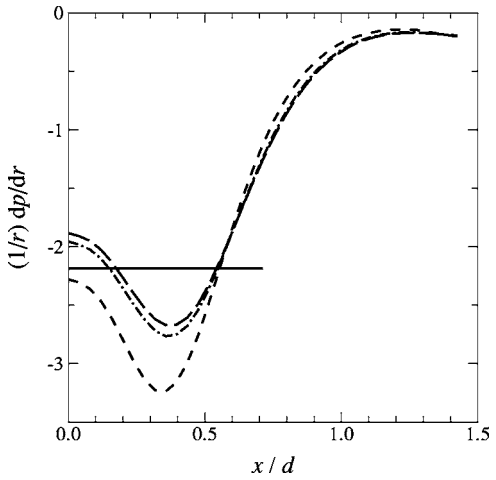

FIG. 19. Comparison of the radial-pressure eigenvalue profile at several radial locations, $r/R=0$ (long-dashed line), $r/R=0.2$ (dash-dotted line), and $r/R=0.5$ (dashed line), to that of the one-dimensional model (solid line), which is constant in both x and r.

ACKNOWLEDGMENTS

We would like to thank D. Lang for his contributions to the digital-imaging in this work, as well as G. Katzenstein for his assistance with experimental design and assembly. R. D. Henderson and H. Blackburn provided considerable assistance, as well as the codes that our axisymmetric viscous simulation code is based on. The work was funded by AFOSR Grant No. F49620-01-1-0006 and the DOE Caltech ASC Contract No. W-7405-ENG-48, whose support is gratefully acknowledged.

APPENDIX A: RADIAL-PRESSURE EIGENVALUE

The one-dimensional formulation for stagnation flows relies on the introduction of a stream function to reduce the axisymmetric Navier-Stokes equations to a third-order ordinary differential equation. One of the assumptions used to derive this simplified model is that the radial-pressure eigenvalue $\Lambda=(1/r)\mathrm{d}p/\mathrm{d}r$ must be a constant. In their study of cold and reacting opposed-jet flow, Frouzakis *et al.* [13] found that this quantity varies in the axial direction when the inlet axial velocity varies radially, while it is close to constant if plug-flow boundary conditions are specified. These authors found that the average value of Λ was approximately equal to that of the corresponding one-dimensional simulations. Figure 19 plots Λ as a function of the axial coordinate at several radii from the present axisymmetric-viscous simulations of impinging-jet flow at Re=700. It can be seen that the radial-pressure eigenvalue is nowhere constant in this flow, even for small x/d where the one-dimensional model appears to yield reasonable agreement with experiment. Near the axis, the radial-pressure eigenvalue is only a function of the axial direction and the radial variation is small. The good agreement between the one-dimensional simulations and either experimental data or two-dimensional simulations indicates that, for this flow, the axial velocity is not sensitively dependent on the spatial variation of Λ.

APPENDIX B: WALL BOUNDARY-LAYER THICKNESS

From one-dimensional stagnation flow theory, the wall boundary-layer thickness is dependent only on the velocity gradient in the potential-flow region [17,18]. The solution to the boundary-layer equations is a linear function in the far field, with a viscous boundary layer close to the wall. The only free parameter in this flow is the far-field velocity gradient U'_∞. In the far field, the high-order derivatives vanish $(U''', U'' \to 0)$ and, from Eq. (9), the radial pressure gradient eigenvalue is equal to $\Lambda/\rho = -(U'_\infty)^2/4$. The resulting equation can be nondimensionalized through the transformations $\xi = x\sqrt{U'_\infty/\nu}$ and $\phi = U(x)/\sqrt{U'_\infty \nu}$, resulting in the following equation for $\phi(\xi)$:

$$2\phi''' - 2\phi\phi'' + (\phi')^2 = 1. \tag{B1}$$

The boundary conditions are $\phi(0) = \phi'(0) = 0$ and $\phi'(\infty) = 1$. Equation (B1) can be solved using a shooting method, where $\phi''(0)$ is adjusted to satisfy the boundary condition at infinity.

Figure 20 shows the solution to Eq. (B1). The nondimensionalized wall boundary-layer displacement thickness δ_ξ can be calculated in the linear region of the flow ($\xi > 5$),

$$\delta_\xi = \xi - \frac{\phi(\xi)}{\phi'(\xi)} = 0.80. \tag{B2}$$

Using Eq. (13), the velocity gradient can be computed at any point on the axis using the error-function fit

$$\frac{\mathrm{d}u(x)}{\mathrm{d}x} = \frac{2U_\mathrm{B}\alpha}{\sqrt{\pi}d} \exp\left[-\alpha^2 \left(\frac{x}{d} - \frac{\delta}{d} \right)^2 \right]. \tag{B3}$$

This yields a maximum velocity gradient of $2U_\mathrm{B}\alpha/(\sqrt{\pi}d)$ at $x = \delta$. Therefore, the slope of the error function as it approaches the boundary layer is given by $\mathrm{d}u/\mathrm{d}x = 2U_\mathrm{B}\alpha/(\sqrt{\pi}d)$. Equating this to U'_∞ allows the boundary-layer thickness to be determined analytically from the other error-function parameters U_B and α. Thus, the wall boundary-layer displacement thickness in physical space is equal to

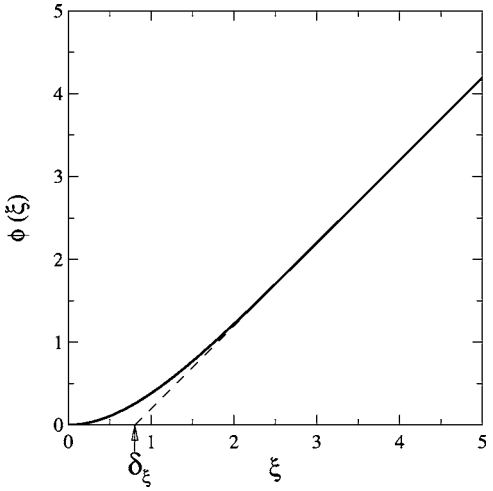

FIG. 20. One-dimensional stagnation flow solution with potential-flow boundary conditions (solid line) and linear fit (dashed line) showing wall boundary-layer offset δ_ξ.

$$\frac{\delta}{d} = \delta_\xi \frac{(\pi)^{1/4}}{(2)^{1/2}} \sqrt{\frac{1}{\mathrm{Re}\,\alpha}} = 0.755 \sqrt{\frac{1}{\mathrm{Re}\,\alpha}}, \tag{B4}$$

where $\mathrm{Re} = dU_\mathrm{B}/\nu$, as defined previously. Since α scales as $\alpha = \alpha_\infty + C_1/\mathrm{Re}$, $\delta/d = 0.755/\sqrt{\mathrm{Re}\alpha_\infty + C_1}$.

[1] A. Rubel, AIAA J. **21**, 351 (1983).
[2] M. D. Deshpande and R. N. Vaishnav, J. Fluid Mech. **114**, 213 (1982).
[3] C. Houtman, D. Graves, and K. Jensen, J. Electrochem. Soc. **133**, 961 (1986).
[4] D. G. Goodwin, in *Proceedings of CVD XVI and EuroCVD Fourteen*, edited by M. D. Allendorf, F. Maury, and F. Teyssandier, (Electrochemical Society, New York, 2003), pp. 155–162.
[5] H. W. Smith, R. A. Schmitz, and R. G. Ladd, Combust. Sci. Technol. **4**, 131 (1971).
[6] M. Fang, R. A. Schmitz, and R. G. Ladd, Combust. Sci. Technol. **4**, 143 (1971).
[7] J. M. C. Mendes-Lopes, Ph.D. thesis, Cambridge University, 1983.
[8] J. M. Bergthorson, D. G. Goodwin, and P. E. Dimotakis, Proc. Combust. Inst. **30**, 1637 (2005).
[9] J. M. Bergthorson, Ph. D. thesis, California Institute of Technology, 2005.
[10] R. J. Kee, J. A. Miller, G. H. Evans, and G. Dixon-Lewis, Sym. (Int.) Combust., [Proc.] **22**, 1479 (1988).
[11] J. C. Rolon, D. Veyante, J. P. Martin, and F. Durst, Exp. Fluids **11**, 313 (1991).
[12] L. W. Kostiuk, K. N. C. Bray, and R. K. Cheng, Combust. Flame **92**, 377 (1993).
[13] C. E. Frouzakis, J. Lee, A. G. Tomboulides, and K. Boulouchos, Sym. (Int.) Combust., [Proc.] **27**, 571 (1998).
[14] C. C. Landreth and R. J. Adrian, Exp. Fluids **9**, 74 (1990).
[15] P. E. Dimotakis, F. D. Debussy, and M. M. Koochesfahani, Phys. Fluids **24**, 995 (1981).
[16] T. Echekki and M. G. Mungal, Sym. (Int.) Combust., [Proc.] **23**, 455 (1990).
[17] H. Schlichting, *Boundary Layer Theory* (McGraw-Hill, New York, 1960).
[18] R. J. Kee, M. E. Coltrin, and P. Glarborg, *Chemically Reacting Flow—Theory & Practice* (John Wiley & Sons, Hoboken, NJ, 2003).
[19] D. J. Phares, G. T. Smedley, and R. C. Flagan, Phys. Fluids **12**, 2046 (2000).
[20] W. Schach, Ing.-Arch. **6**, 51 (1935).
[21] T. Strand, AIAA Pap. **64**, 424 (1964).
[22] R. D. Henderson and G. E. Karniadakis, J. Comput. Phys. **122**, 191 (1995).
[23] G. E. Karniadakis and S. J. Sherwin, *Spectral/hp element*

methods for CFD (Oxford University Press, New York, 1999).
[24] G. Birkhoff and E. H. Zarantonello, *Jets, Wakes and Cavities* (Academic Press, New York, 1957).
[25] M. I. Gurevich, *Theory of Jets in Ideal Flows* (Academic Press, New York, 1965).
[26] A. T. Patera, J. Comput. Phys. **54**, 468 (1984).
[27] A. Leonard and A. Wray, in *Proceedings of the Eighth International Conference on Numerical Methods in Fluid Dynamics*, edited by E. Krause, *Lecture Notes in Physics*, Vol. 170 (Springer-Verlag, New York, 1982), pp. 335–342.
[28] G. K. Batchelor, *An Introduction to Fluid Dynamics* (Cambridge University Press, New York, 1967).